Two-dimensional cuprate nanodetector with single telecom photon sensitivity at T = 20 K

2D Materials

CrossMark

OPEN ACCESS

RECEIVED
26 October 2022

REVISED
11 January 2023

ACCEPTED FOR PUBLICATION
19 January 2023

PUBLISHED
9 February 2023

LETTER

Two-dimensional cuprate nanodetector with single telecom photon sensitivity at $T = 20$ K

Rafael Luque Merino[1,8,9,*], **Paul Seifert**[1,2], **José Durán Retamal**[1,3], **Roop K Mech**[1,8,9], **Takashi Taniguchi**[4], **Kenji Watanabe**[5], **Kazuo Kadowaki**[6], **Robert H Hadfield**[7] and **Dmitri K Efetov**[1,8,9,*]

[1] ICFO—Institut de Ciencies Fotoniques, The Barcelona Institute of Science and Technology, Castelldefels, Barcelona 08860, Spain
[2] Institute of Physics, Faculty of Electrical Engineering and Information Technology (EIT 2), Universität der Bundeswehr München, Neubiberg 85577, Germany
[3] Catalan Institute of Nanoscience and Nanotechnology (ICN2), BIST & CSIC, Barcelona 08193, Spain
[4] International Center for Materials Nanoarchitectonics, National Institute for Materials Science, 1-1 Namiki, Tsukuba 305-0044, Japan
[5] Research Center for Functional Materials, National Institute for Materials Science, 1-1 Namiki, Tsukuba 305-0044, Japan
[6] University of Tsukuba, 1-1-1 Tennodai, Tsukuba-shi 305-8572, Japan
[7] James Watt School of Engineering, University of Glasgow, Glasgow, United Kingdom
[8] Fakultät für Physik, Ludwig-Maximilians-Universität, Schellingstrasse 4, 80799 München, Germany
[9] Munich Center for Quantum Science and Technology (MCQST), München, Germany
[*] Authors to whom any correspondence should be addressed.

E-mail: rafael.luque@icfo.eu and dmitri.efetov@lmu.de

Keywords: 2D, cuprate, nanodetector, telecom, photon, nanowire, He-FIB

Supplementary material for this article is available online

Abstract

Detecting light at the single-photon level is one of the pillars of emergent photonic technologies. This is realized through state-of-the-art superconducting detectors that offer efficient, broadband and fast response. However, the use of low T_C superconducting thin films limits their operation temperature to approximately 4 K and below. Here, we demonstrate proof-of-concept nanodetectors based on exfoliated, two-dimensional cuprate superconductor $Bi_2Sr_2CaCu_2O_{8-\delta}$ that exhibit single-photon sensitivity at telecom wavelength at a record temperature of $T = 20$ K. These non-optimized devices exhibit a slow ($\sim ms$) reset time and a low detection efficiency ($\sim 10^{-4}$). We realize the elusive prospect of single-photon sensitivity on a high-T_C nanodetector thanks to a novel approach, combining van der Waals fabrication techniques and a non-invasive nanopatterning based on light ion irradiation. This result paves the way for broader application of single-photon technologies, relaxing the cryogenic constraints for single-photon detection at telecom wavelength.

Superconducting nanowire single-photon detectors (SNSPD's) constitute an established technology for broadband, sensitive and fast detection of faint optical signals [1–3]. These detectors, based on low T_c superconducting thin films such as NbN or WSi, provide high efficiency [4], fast response ($\sim$ ns) [2, 3] and excellent timing resolution ($\sim$ ps) [5]. SNSPD's can be integrated in free-space and fiber-coupled architectures [1, 2], as well as planar photonic circuits [6, 7]. However, their operating temperature is usually limited to $T \leq 4$ K by the T_c of the thin films. To date, the highest operating temperature for an SNSPD is 11 K, demonstrated in a MgB_2 nanostrip [8]. Expanding single-photon detection to higher operating temperatures, longer wavelengths and faster response motivates the search for new material platforms [9–11]. In particular, van der Waals (vdW) heterostructures of 2D materials [12–15] and high-T_c superconductors [9, 16–24] have received interest as candidates for the development of next-generation SNSPD's with increased capabilities.

Cuprate superconductors are natural candidates to push SNSPD technology to higher temperatures [9]. A cuprate-based SNSPD could operate above liquid nitrogen temperatures (77 K) offering a critical technological advantage. Fabrication of cuprate detectors has proven to be very challenging, as cuprates degrade rapidly under ambient conditions. Despite extensive research efforts, most cuprate nanostructures exhibit flux-flow behaviour characterized by smooth current–voltage (I–V)

characteristics that preclude SNSPD operation [16, 22, 23]. Sharp and hysteretic transport characteristics, as those of conventional SNSPD thin films, were reported for high-quality $YBa_2Cu_3O_{7-\delta}$ (YBCO) nanowires along with the observation of dark counts [18, 19, 21]. To date, conventional fabrication approaches based on lift-off methods or heavy ion milling have not realized the prospect of a cuprate SNSPD.

We explore an alternative approach based on exfoliated, 2D cuprate $Bi_2Sr_2CaCu_2O_{8-\delta}$ (BSCCO). Novel fabrication methods allow us to harness the pristine superconducting properties of few-layer BSCCO [24–26]. We report multiple nanostructures with sharp, hysteretic *I–V* characteristics combined with high T_c (70–80 K). Optoelectronic measurements of the BSCCO nanostructures reveal single-photon sensitivity up to a record temperature of $T = 20$ K. The detection speed and efficiency remain low for these proof-of-concept cuprate nanodetectors.

1. Results and discussion

1.1. Device fabrication and transport characterization

Figure 1(a) summarizes the detector concept and fabrication. We fabricate vdW heterostructures of few-layer BSCCO encapsulated with a top hBN inside an Ar-filled glovebox [27]. We use a bottom contact approach with thin metallic electrodes to bypass lift-off methods, which lead to oxidation of few-layer BSCCO. In order to preserve superconductivity in BSCCO nanostructures, we use a helium focused ion beam (He-FIB) to pattern our BSCCO/hBN heterostructures [28]. The doping level (and electronic properties) of few-layer BSCCO can be locally modified by light He-ion irradiation [29–31]. Direct patterning of insulating BSCCO areas can restrict the supercurrent to flow exclusively along channels of crystalline, non-irradiated BSCCO that preserve high T_c. Importantly, for low ion doses the He-FIB irradiation does not etch through the encapsulating hBN layer (see figure S4). This non-invasive patterning technique allows us to produce high-quality nanostructures based on 2D BSCCO flakes that remain protected by the encapsulating hBN. This method also provides very high lateral resolution, allowing the writing of complex patterns with $\sim$ nm resolution. The left inset in figure 1(a) shows an scanning electron microscopy (SEM) image of a He-FIB defined nanostructure in our BSCCO/hBN stacks. This device is 250 nm wide and 2.7 μm long. See Methods and sections S1 and S2 of the SI for further details on the device fabrication.

We study the transport properties of the fabricated BSCCO nanostructures and compare them to pristine BSCCO flakes. In figure 1(b) we present temperature dependent measurements of the two-terminal resistance *R*, normalized to its value at 120 K (R_{120K}) for three BSCCO/hBN nanopatterned detectors and an exfoliated, unpatterned BSCCO flake (reference sample). All the curves show clear superconducting transitions, where R/R_{120K} drops to close to 0 resistance, with a residual resistance value stemming from the contact resistance in this two-terminal device. The critical temperature of the BSCCO nanostructures T_c, defined from the mid-point of the superconducting transition, ranges between 60 and 80 K. The lowered T_c and broadened SC transition of the patterned flakes likely derive from microscopic disorder and/or He-ion implantation [30, 31]. Still, the critical temperatures remain close to their nominal value and near liquid nitrogen temperatures. The upturn of the resistance below T_c stems from contact resistance at the BSCCO/Au interface forming a Schottky barrier. For two-terminal measurements with low excitation current (10–100 nA in this measurement) the contact resistance contribution becomes sizable. When applying a DC offset current, as done below, this Schottky barrier is greatly lowered.

Figure 1(c) shows the *I–V* characteristics of the BSCCO nanostructures for different temperatures, and the inset shows the corresponding colour plot for the full temperature range. The *I–V* curve at $T = 10$ K features an abrupt transition to the resistive state at a critical current. The combination of high T_c and low critical current I_c proves that the nano-patterning confines the supercurrent into a narrow, pristine BSCCO channel, as the intrinsic I_c for an unpatterned BSCCO flake is several orders of magnitude larger. The critical current density of the nano-constriction is $J_C \sim 7x10^6$ A cm^{-1}, comparable to previous reports on high-quality nanowires based on YBCO thin films [18, 19]. The appearance of a single, well-defined voltage jump at I_c reflects a robust superconducting state of the undamaged channel in the BSCCO nanoconstriction. As *T* increases, the *I–V* characteristics become flux-flow like. However remarkably, the sharply transition at I_c persists up to $T = 30$ K.

Strikingly we observe a strong hysteresis in the *I–V* curves with respect to the sweeping direction of the bias current I_b, as shown in figure 1(d) at $T = 20$ K. As *I* is decreased below I_c, the superconducting state in the nanostructure is not recovered. Instead, the nanowire switches back into its superconducting state at a lower retrapping current I_r. The occurrence of the hysteresis is a linked to the sharp *I–V* characteristics at I_c and the high normal state resistance in the BSCCO nanostructure [18–21]. It also intricately depends on the thermal properties of the superconducting devices [20]. In our nano-structured BSCCO constrictions, the thermal conductance is reduced both in-plane, across the disordered irradiated BSCCO regions [30],

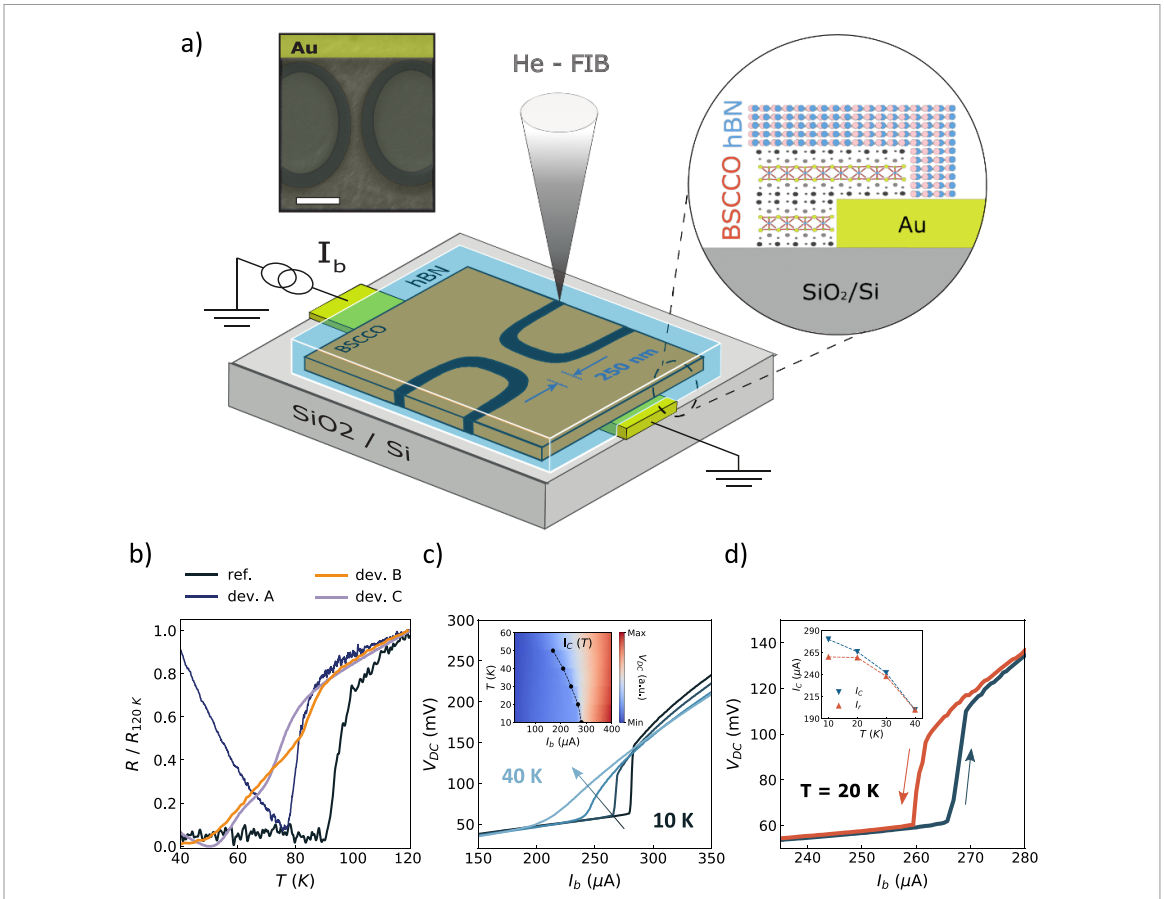

Figure 1. Two-dimensional superconducting cuprate nanowires for photodetection. (a) Illustration of the detector concept. A high-T_c superconducting BSCCO flake is encapsulated with hBN and then nanopatterned using a focused He-ion beam. The resulting nanostructure is current-biased (I_b) in a two-terminal configuration. Left inset shows an SEM image of the nanowire in Device A, scale bar has 1 μm length. Right inset depicts a schematic cross-section of the vdW heterostructure. (b) Two-terminal resistance vs. temperature of the BSCCO nanostructures. All curves have been normalized to the resistance value at 120 K, before the superconducting transition. Black curve shows the four-terminal resistance for a reference, unpatterned BSCCO flake. For all nanostructures, T_c ranges between 60–80 K. (c) I–V characteristics of device A for increasing temperature. The abrupt voltage jump at 10 K evolves towards a smooth transition at 40 K. Inset depicts the superconducting phase diagram for this device. Overlayed plot indicates the extracted I_c (T) dependence. Beyond 50 K, the smooth I–V characteristics preclude a reliable extraction of I_c. (d) I–V characteristic for device A at $T = 20$ K, exhibiting a sharp voltage jump along with a well-defined hysteresis loop. Vertical offset between red and blue traces is due to Joule heating effects in the DC measurement. Inset shows I_c (T) and I_r (T). Hysteresis loop remains finite up to $T = 30$ K.

and out-of-plane, as the 2D flake lies on the substrate without any lattice matching [32]. Figure S5 in the SI demonstrates the ubiquity of hysteretic behaviour in these nanostructures.

Such hysteretic behaviour is a key requirement for SNSPD. The nucleation of a self-sustaining resistive region after photo-absorption induces Joule heating, precluding the recovery of the superconducting state when approaching I_c from above. Superconducting nanowire detectors are kept well below T_c and biased close to their critical current $I_b \sim I_c$. Photo-induced hotspots are nucleated and grow due to Joule heating leading to a thermal runaway of the detector, which latches into the resistive state until the bias current is shunted [33]. Thus, a voltage drop takes place in the shunting circuit due to the resistive switching of the nanodetector. Remarkably, the observed hysteretic behaviour of the BSCCO nano-constrictions persists up to $T = 30$ K (see figure 1(d)) highlighting their potential as superconducting nanodetectors with single photon sensitivity and high operating temperature.

1.2. Photo-induced switching events in the BSCCO nanostructure

We now characterize the optoelectronic response of the BSCCO nano-constriction at a temperature of $T = 20$ K, where figure 2(c) shows a sketch of the readout circuit and section 5 of the SI illustrates the complete optoelectronic setup. The BSCCO nano-constriction is current-biased close to its switching current $I_b \sim 0.97\, I_c$ and connected in parallel to a load resistor R_{Load}. The load resistor shunts the current once the nanostructure turns resistive, and enables free-running detection as the device self-resets after a time τ. We illuminate the biased BSCCO nanodetector using a CW laser at a telecom wavelength of $\lambda = 1550$ nm, and monitor the voltage drop across

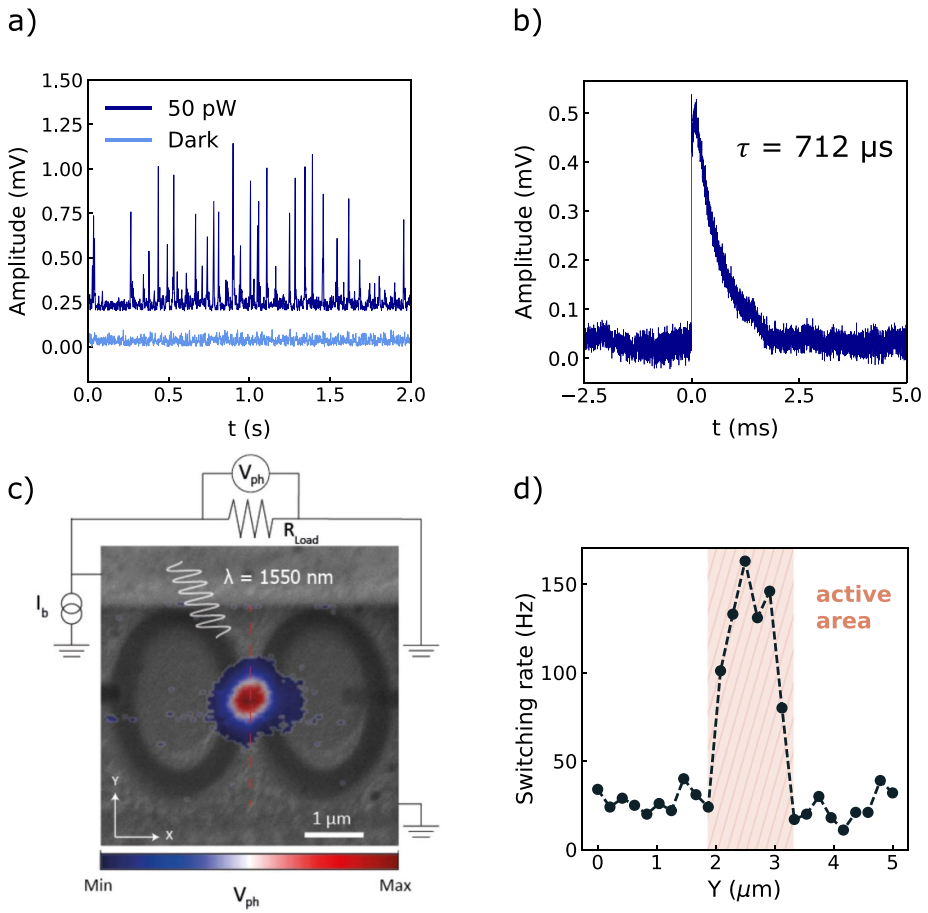

Figure 2. Photo-induced voltage signal in Bi2212 nanowires. (a) Photo-induced voltage drop at the load resistor over time for 50 pW optical power (black) and under no illumination (grey). Black trace is offset by 0.2 mV for clarity. Traces recorded at $T = 10.8$ K, $I_b = 0.98\ I_c$. (b) Oscilloscope trace of the voltage trace generated by a switching event. The obtained decay time is $\tau = 712\ \mu$s. Switching rate of the detector along the red dashed line in (a). Optoelectronic measurement schematic and spatial photovoltage map, overlayed with SEM image of the nanowire. The nanowire is biased close to its critical current $I_b \sim I_c$. (d) Switching rate of the detector along the red dashed line in (**c**).

R_{Load} over time. We observe clear photo-induced clicks that appear only at elevated photon fluxes are absent in dark conditions. Figure 2(a) illustrates the appearance of these switching events under laser illumination.

Using an oscilloscope we measure the time-domain traces of the photo-induced clicks. We find that each click (figure 2(b)) features a fast rise time (few μs) and a slow decay time $\tau = 712\ \mu$s, obtained fitting the falling edge of the pulse. The full recovery time of the device lasts about 2 milliseconds. The observed τ is much slower than the reset time of conventional SNSPD's($\sim$ ns) [2, 3] and the reported intrinsic photoresponse time of cuprate superconductors [26, 34]. This slow relaxation time is consistent across all devices (figure S7).

We believe the observed timescale to be an extrinsic effect, as the hotspot dynamics in a BSCCO nanostructure are expected to be orders of magnitude faster. In previous work, we found the intrinsic thermal relaxation time of BSCCO bolometers to be in the order of nanoseconds [24]. These limitations likely stem from a non-optimized electrical circuit, which does not include a Bias Tee to isolate the bias (DC) and readout (AC) paths. It is worth noting that the contact resistance in these devices also sets some limitations on the choice for parallel load resistors, as well as energy dissipation and capacitance in the contact interfaces that may affect the shunting dynamics.

We identify the photo-active area by scanning the laser beam across the device and measuring with the AC Lock-in technique. As expected, peaks at the narrowest area of the device where the superconducting state is closest to its transition. In figure 2(c), we overlay the photo-voltage mapping V_{ph} with a SEM image of the device. Having located the detector's active area, we now measure its switching rate using a Zurich UHLFI as a fast voltmeter. Figure 2(d) shows the measured switching rate of the detector in a scan across the nano-constriction (indicated by the red dashed line in figure 2(c)). As the laser spot illuminates the 'wings' of the nanostructure, the switching rate is constant and increases five-fold at the nanostructure's narrowest, most sensitive area. The high spatial sensitivity of the switching rate indicates that the clicks do not originate from a heating,

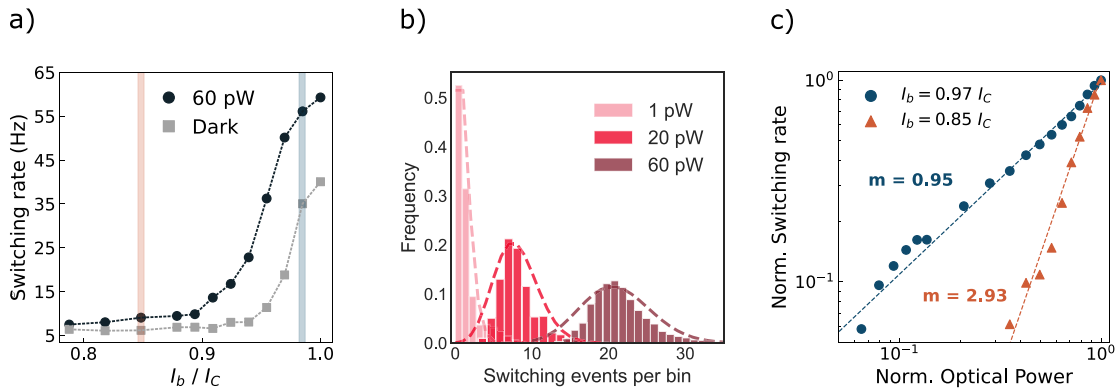

Figure 3. Single photon sensitivity at $T = 20$ K. (a) Switching rate and dark count rate of device A at 20 K for increasing bias current. Vertical segments indicate the bias points examined in (**c**). (b) Distribution of the photo-induced switching events in device A for increasing optical power at 20 K,$I_b = 0.97I_c$. The switching event distribution is consistent with Poissonian statistics of few-photon events. Dashed lines illustrate the best-fitting Poissonian distribution. Each bin is a 60 millisecond time window. (c) Normalized switching rate versus normalized optical power for two different bias conditions. Each magnitude is normalized to its maximum value. The switching statistics for $I_b = 0.97I_c$ follow a linear dependence, indicating single-photon sensitivity of the nanodetector. For $I_b = 0.85I_c$, the switching rate follows a power law of exponent $m \approx 3$, indicating multi-photon sensitivity of device A at lower bias currents. Switching events recorded at 20 K. The maximum switching rate for $I_b = 0.97I_c$ and $I_b = 0.85I_c$ are 450 Hz and 38 Hz, respectively. Maximum optical power is 100 pW.

bolometric effect. Instead, this observation points towards Cooper pair breaking and a subsequent avalanche effect leading to nanowire switching.

1.3. Statistics of the switching events and single-photon sensitivity

We characterize the sensitivity of our BSCCO nanodetectors by studying the switching rate as a function of applied bias current I_b and incident optical power P. All following measurements are performed at $T = 20$ K. In order to reliably discern switching events from the noise floor, we define a voltage threshold based on the detector's switching statistics under no illumination at each I_b. The following discussion is consistent for different choices of this threshold. The protocol to define the threshold is further detailed in section S7 of the SI.

First, we fix the optical power on the detector and vary the applied bias current I_b. For SNSPD-type detectors, the sensitivity and detection efficiency strongly depend on I_b, increasing as I_b approaches I_c. These detectors reach single-photon sensitivity for I_b I_c, at the cost of increased false counts due to thermal fluctuations and/or stray photons. Figure 3(a) shows the switching rate of the detector for increasing I_b under $P = 60$ pW illumination and in dark conditions. We find that the switching rate of our BSCCO nanowire rapidly grows for $I_b \geqslant 0.9\ I_c$. A full saturation of the detector's switching rate, indicative of full internal quantum efficiency, was not observed. The growth of the switching rate slows down significantly for $I_b \geqslant 0.97\ I_c$, suggesting that a full saturation could be achieved. The non-saturating switching rate is common in nanoconstriction detectors where the device geometry leads to a position-dependent I_c. Thus, as I_b is increased the effective active area of the nanodetector changes and the switching rate does not fully saturate [35, 36].

The bias current dependence of the dark switching events resembles that of the total switching rate. This suggests that the dark count rate stems from the absorption of stray photons, likely coming from the thermal emission from the room-temperature objective. As the bias current is increased, the switching rate grows surpasses the dark switching rate as the detector becomes more sensitive to the high flux of 1550 nm photons.

We analyze the statistics of the observed switching events fixed temperature of $T = 20$ K and for varying optical powers and bias current configurations. We record switching events in 5 min windows. The distribution of few-photon detection events in SNSPD's can be described through Poissonian statistics, as the switching events are rare and uncorrelated. In figure 3(b), we illustrate the distribution of switching events at $I_b = 0.97\ I_c$ for increasing optical power. At low optical power (1 pW), very few clicks are observed and the switching events exhibit a highly skewed Poissonian-like distribution. As the optical power is increased, the switching rate of the detector increases and the distribution evolves towards higher mean values μ and variances σ^2. The distribution of the observed clicks is compatible with Poissonian statistics arising from few-photon absorption events in the BSCCO nanodetector. The bins in figure 3(b) correspond to 60 millisecond time windows.

Lastly, we present the power dependence of the switching rate of our BSCCO superconducting nanodetectors. As the sensitivity of SNSPD-type detectors depends strongly on the applied bias current [36, 37], we study the sensitivity of our devices at two different bias conditions, highlighted by the vertical colored segments in figure 3(a). The low-bias

condition (orange) corresponds to $I_b = 0.85\, I_c$ and the high-bias condition (blue) is $I_b = 0.97\, I_c$.

Figure 3(c) shows the power dependence of the switching rate in the high and low-bias conditions. The few-photon sensitivity of an SNSPD-type detector can be inferred from the power dependence of its switching rate. The probability to detect k photons (switching event caused by simultaneous absorption of k photons) is given by $P[k] \propto e^{-\lambda}\lambda^k/k!$, where λ is the mean (absorbed) photon number in the detector per unit time. For a single-photon detector the switching rate should increase linearly with incident power $P[k=1] \propto \lambda$. We observe a linear ($m = 0.95 \approx 1$) power dependence of the switching rate in the high-bias condition ($I_b \sim 0.97\ I_c$). When the bias current is lowered, the switching rate of the BSCCO detector is strongly reduced and exhibits a markedly different dependence. For low bias ($I_b \sim 0.85\ I_c$), the dependence falls closer to a power law of exponent $m = 2.93 \approx 3$, indicative of multi-photon (two and three-photon) events dominating the detector's response. Extended data supporting this observation is presented in section 8 of the SI.

This behaviour is consistent with a single-photon sensitivity of the BSCCO nano-constrictions at $T = 20$ K for telecom photons, where the observation of multi-photon sensitivity at lower bias current further supports the SNSPD-like characteristics of the BSCCO nanodetectors [36, 37]. As discussed before, far from the superconducting transition, the energy deposited by a single absorbed photon is not enough to trigger a switching event and multiple simultaneous photons need to be absorbed. Multi-photon sensitivity is rarely observed in commercial SNSPD's, as large fill factor designs make simultaneous absorption of multiple photons in the same area extremely unlikely. Instead, for detectors featuring constrictions, these events are more prominent and their photon sensitivity is strongly bias-dependent [36]. In our case, the CW nature of the illumination also promotes multi-photon contributions to the switching rate.

The detection efficiency can be roughly estimated using the incident power, number of switching events and the optical cross-section of the detector. Further details on the efficiency estimation are provided in section S11 of the SI. In the high-bias condition where single-photon sensitivity is observed, we estimate a lower bound for the detector efficiency of $\eta \approx 3.3 \times 10^{-4}$. Several factors may contribute to this low figure-of-merit: (a) due to the large superconducting gap of BSCCO, the energy of a single telecom photon would only break around a dozen Cooper pairs. The resulting quasiparticle generation process that leads to a resistive switching may therefore not be efficient [38]. (b) the effective (electronic) width of the active region may be smaller than estimated, as the microscopic details of the irradiation are unknown. (c) Another plausible scenario is the existence of a highly efficient, nanometric region inside the detector where photodetection takes place. Assuming an absorption coefficient of 17% [39] and full quantum efficiency, we can estimate the area of such a region to be $\sim 80\ \mathrm{nm}^2$. This scenario is reminiscent of switching events around local microscopic defects and cannot be ruled out.

The microscopic details of the physical processes occurring after photo-absorption in the BSCCO nanostructures remain an open question. Even though our experiment does not probe the detection mechanism of this system, our results are consistent with an agnostic hotspot model. In this scenario the photon energy is absorbed by the superconducting condensate, locally breaking Cooper pairs. The Cooper pair density is suppressed in the hotspot, precluding the supercurrent from flowing across the full width of the nanostructure. The hotspot grows through avalanche effect due to Joule heating, eventually causing the entire nanowire width to become resistive. This avalanche effect can give rise to macroscopic voltage signals from a microscopic perturbation (single-photon absorption).

The observation of strong hysteresis in the I–V characteristics of our nanodetectors supports the nucleation of a self-sustaining hotspot. We observe complete latching of the nanodetector after photo-absorption in the absence of a shunting circuit, proving that the avalanche effect can be triggered optically. In literature, hotspots in cuprate thin films have been observed directly through thermal imaging [40] and indirectly through transport measurements [41, 42]. The large thermal conductivity κ of cuprates has limited cuprate nanostructures to the flux-flow regime, where an avalanche effect does not take place and ultimate sensitivity cannot be achieved. Suppression of the thermal conductance in these 2D vdW nanostructures could explain the existence of a self-sustaining hotspot. This behaviour is not expected for Au-capped thin films studied in other reports [16, 18].

We believe that tailoring of thermal and electronic properties will be key for developing next-generation quantum sensors based on cuprate nanostructures. Achieving this while preserving the superconducting properties of the material may prove challenging. Possible advances of the device fabrication are discussed in section 4 of the SI. Other avenues to enhance detector performance include the design of optical gratings and nanoantennas to boost the absorption in the material. The integration in planar photonic architectures, highly compatible with 2D materials, could also boost the device's efficiency [6, 7, 24]. Lastly, the material properties of BSCCO also show promise for detection of single-photons at shorter wavelengths, as well as its application for photodetectors resilient to high magnetic fields [43].

In summary, we report single-photon sensitivity at $T = 20$ K for telecom photons in nanostructures based on exfoliated 2D cuprate superconductor BSCCO. This proof-of-concept nanodetector sets the highest operation temperature reported to date for an SNSPD-type detector, establishing BSCCO-based vdW nanostructures as a promising platform for next-generation quantum sensors.

2. Note

During the elaboration of this text, we became aware of a similar work published in arXiv after ours. This complementary work by Charaev *et al* employs similar fabrication methods, highlighting the potential for next-generation SNSPD's based on high-temperature superconductors. The reference is Charaev *et al* arXiv:2208.05674 (2022).

3. Methods

3.1. Device fabrication

We fabricate our samples through the dry-transfer technique inside an Ar-filled glovebox (H_2O, $O_2 < 0.8$ ppm). Few-layer flakes of optimally doped BSCCO (10–20 nm) are exfoliated using polydimethylsiloxane (PDMS) stamps, then transferred onto pre-patterned metallic electrodes (Ti/Au, 2/20 nm). BSCCO flakes are then encapsulated using pre-selected thin hBN flakes ($\sim$ 20 nm). We probe the two-terminal resistance of our devices using a probe-station inside the glovebox. The entire process is performed in less than 20 min to avoid degradation of few-layer BSCCO flakes. The entire vdW assembly process is done at room temperature.

The chip is then pasted onto a stub for He-FIB using silver paste and the contacts of the device are bonded onto the metallic stub, so the entire device remains grounded during patterning. Outside the glovebox, the devices are always in vacuum using a commercial vacuum container. Therefore, the device is only exposed momentarily, for example during bonding.

In the He-FIB we work with 30 KeV acceleration voltage for the Helium beam, and typical emission currents between 2–5 pA. For each sample, we calibrate the optimal He ion dose in order to locally turn BSCCO insulating. This process is discussed in section 2 of the SI, as well as in [22]. Typical ion doses range between 20–90 pC μm^{-2}. Crucially, for low ion doses, the Helium ion beam does not etch through the encapsulating hBN layer so the BSCCO flakes remain protected. We fabricate simple nanowires as well as complex structures (see section 1 of the SI). Lastly, we remove the sample from the metallic stub and bond the chip to a pre-grounded PCB. The PCB is then loaded into our optical cryostat.

Our devices are typically kept in the cryostat for 2–4 week measurement runs. Careful thermal cycling can preserve the detector's SC properties. Prolonged exposure to air leads to oxidation due to oxygen out-diffusion and water creep through the SiO_2 roughness.

3.2. Transport and optoelectronic setup

We characterize the optoelectronic properties of the vdW BSCCO nanowires using an Attodry800 optical cryostat with a base temperature of 8 K. We maintain a temperature of 20 K on the sample using a standard calibrated microheater + Cernox thermometer combination. We ensure proper thermalization of the sample with the cryostat's cold finger.

For transport characterization, we perform both AC Lock-in measurements and DC measurements. For the AC Lock-In measurements, we use a 10 nA AC excitation current at a reference frequency of 126 Hz. An SRS860x Lock-In amplifier is used both for sourcing and sensing. DC measurements are performed using a combination of DC sources (Yokogawa GS200, Keithley 2450) and a multimeter (Keithley 2700). It is worth noting that for Device C, the normal state resistance is very large ($\sim$100 KΩ), making a voltage bias circuit favourable over a current bias circuit.

Laser excitation is provided by a telecom CW diode laser (Thorlabs SFL1550P), driven by a DC current source (Keithley 2400). The laser beam is first attenuated using neutral density filters. Then, it is aligned and focused onto the sample using a combination of room-temperature galvanic mirrors and a cryogenic three-axis piezo stage for the sample. At optimal focus, the laser has a beam width of $w_0 \sim 2$ μm. The optical power is measured using a power meter. We calibrate the laser excitation power in the range between 10 nW and 1 μW. Then we introduce a neutral density filter of density $D = 4$ in the optical path, which attenuates the optical power by four orders of magnitude.

The detector is current-biased, connected in parallel to a load resistor. The voltage drop at the load resistor generated by the detector's resistive switching is recorded using a Zurich UHFLI (10 MΩ input impedance, 600 MHz bandwidth, 1.8 GSa s^{-1} sampling rate). A low-noise amplifier with 45 dB gain and bandwidth between 100 Hz and 100 KHz is used to pre-amplify the voltage spikes. The Zurich UHLFI records switching events for 5 min at each optical power and bias current setting. Time—domain traces of the switching events are recorded using the oscilloscope function of the Zurich UHFLI with a sampling rate of 175 MHz. Alternatively, we study the photovoltage signal of the device using an optical chopper and a Lock-In amplifier (SRS860x) referenced at the chopper frequency. Optimizing the optical coupling to the detector becomes easier in this 'slower'

configuration (see figure 2(c)). A schematic of the optoelectronic setup for single-photon detection is shown in figure S6.

Data availability statement

The data that support the findings of this study are available upon reasonable request from the authors.

Acknowledgments

R L M acknowledges fruitful discussions with Giorgio di Battista and support with the He-FIB by Hanan Herzig Sheinfux, Johann Osmond and Helena Lozano. D K E acknowledges support from the Ministry of Economy and Competitiveness of Spain through the 'Severo Ochoa' program for Centres of Excellence in R&D (SE5-0522), Fundació Privada Cellex, Fundació Privada Mir-Puig, the Generalitat de Catalunya through the CERCA program, the H2020 Programme under Grant Agreement No. 820378, Project: 2D × SIPC and the La Caixa Foundation. K W and T T acknowledge support from the Elemental Strategy Initiative conducted by the MEXT, Japan, Grant No. JPMXP0112101001, JSPS KAKENHIGrant No. JP20H00354 and the CREST (JPMJCR15F3), JST P S acknowledges support from the Alexander-von-Humboldt Foundation and the German Federal Ministry for Education and Research through the Feodor-Lynen program. R L M acknowledges that this Project has received funding from the "Secretaria d'Universitats I Recerca de la Generalitat de Catalunya, as well as the European Social Fund (L'FSE inverteix en el teu futur)—FEDER.

Author contributions

D K E, P S and R L M conceived and designed the experiments; R L M and P S performed the experiments; R L M, J R D and P S fabricated the devices; R L M and D K E analyzed the data; K K, T T, K W contributed materials; R M and D K E supported the experiments: R L M and D K E wrote the paper with insight from R H H.

ORCID iDs

Kenji Watanabe https://orcid.org/0000-0003-3701-8119
Robert H Hadfield https://orcid.org/0000-0002-8084-4187
Dmitri K Efetov https://orcid.org/0000-0001-5862-0462

References

[1] Morozov D V, Casaburi A and Hadfield R H 2021 Superconducting photon detectors *Contemp. Phys.* **62** 69–91
[2] Holzman I and Ivry Y 2019 Superconducting nanowires for single-photon detection: progress, challenges, and opportunities *Adv. Quantum Technol.* **2** 1800058
[3] Gol'tsmann G N, Okunev O, Chulkova G, Lipatov A, Semenov A, Smirnov K, Voronov B, Dzardanov A, Williams C and Sobolewski R 2001 Picosecond superconducting single-photon optical detector *Appl. Phys. Lett.* **79** 705–7
[4] Marsili F *et al* 2013 Detecting single infrared photons with 93% system efficiency *Nat. Photon.* **7** 210–4
[5] Korzh B *et al* 2020 Demonstration of sub-3 ps temporal resolution with a superconducting nanowire single-photon detector *Nat. Photon.* **14** 250–5
[6] Pernice W H P, Schuck C, Minaeva O, Li M, Goltsmann G N, Sergienko A V and Tang H X 2012 High-speed and high-efficiency travelling wave single-photon detectors embedded in nanophotonic circuits *Nat. Commun.* **3** 1325
[7] Münzberg J, Vetter A, Beutel F, Hartmann W, Ferrari S, Pernice W H P and Rockstuhl C 2018 Superconducting nanowire single-photon detector implemented in a 2D photonic crystal cavity *Optica* **5** 658
[8] Shibata H, Takesue H, Honjo T, Akazaki T and Tokura Y 2010 Single-photon detection using magnesium diboride superconducting nanowires *Appl. Phys. Lett.* **97** 212504
[9] Santavicca D F 2018 Prospects for faster, higher-temperature superconducting nanowire single-photon detectors *Supercond. Sci. Technol.* **31** 040502
[10] Parlato L *et al* 2017 Investigation of dark counts in innovative materials for superconducting nanostripe single-photon detector applications *Photon Count. Appl.* **10229** 1022901
[11] Lian S J, Cheng B, Cui X and Miao F 2019 Van der Waals heterostructures for high-performance device applications: challenges and opportunities *Adv. Mater.* **32** 1903800
[12] Lee G-H *et al* 2019 Graphene-based Josephson junction microwave bolometer *Nature* **586** 42–46
[13] Walsh E D *et al* 2021 Josephson junction infrared single-photon detector *Science* **372** 409–12
[14] Di Battista G, Seifert P, Watanabe K, Taniguchi T, Fong K C, Principi A and Efetov D K 2022 Revealing the thermal properties of superconducting magic-angle twisted bilayer graphene *Nano Lett.* **22** 6465–70
[15] Orchin G J *et al* 2019 Niobium diselenide superconducting photodetectors *Appl. Phys. Lett.* **114** 251103
[16] Arpaia R, Ejrnaes M, Parlato L, Tafuri F, Cristiano R, Golubev D, Sobolewski R, Bauch T, Lombardi F and Pepe G P 2015 High-temperature nanowires for photon detection *Physica* C **509** 16–21
[17] Xing X, Balasubramanian K, Bouscher S, Zohar O, Nitzav Y, Kanigel A and Hayat A 2020 Photoresponse above 85 K of selective epitaxy grown high-Tc superconducting microwires *Appl. Phys. Lett.* **117** 032602
[18] Arpaia R, Golubev D, Baghdadi R, Ciancio R, Drazic G, Orgiani P, Montemurro D, Bauch T and Lombardi F 2017 Transport properties of ultrathin YBaCuO nanowires: a route to single-photon detection *Phys. Rev.* B **96** 064525
[19] Andersson E, Arpaia R, Trabaldo E, Bauch T and Lombardi F 2020 Fabrication and electrical transport characterization of high quality underdoped $YBa_2Cu_3O_{7-\delta}$ nanowires *Supercond. Sci. Technol.* **33** 064002
[20] Skocpol W J, Beasley M R and Tinkham M 1974 Self-heating hotspots in superconducting thin-film microbridges *J. Appl. Phys.* **45** 4054
[21] Ejrnaes M, Parlato L, Arpaia R, Bauch T, Lombardi F, Cristiano R, Tafuri F and Pepe G P 2017 Observation of dark pulses in 10 nm thick YBCO nanostrips presenting hysteretic current voltage characteristics *Supercond. Sci. Technol.* **30** 12LT02
[22] Lyatti M, Savenko A and Poppe U 2016 Ultrathin $YBa_2Cu_3O_{7-\delta}$ films with high critical current density *Supercond. Sci. Technol.* **29** 065017
[23] Li M, Winkler D and Yurgens A 2015 Single-crystalline $Bi_2Sr_2CaCu_2O_{8+x}$ detectors for direct detection of microwave radiation *Appl. Phys.Lett.* **106** 152601
[24] Ghosh S, Jangade D A and Deshmukh M M 2022 Nanowire bolometer using a 2D high-temperature superconductor *Nanotechnology* **34** 015304

[25] Yu Y, Ma L, Cai P, Zhong R, Ye C, Shen J, Gu G D, Chen X H and Zhang Y 2019 High-temperature superconductivity in monolayer $Bi_2Sr_2CaCu_2O_{8+\delta}$ *Nature* **575** 156–63
[26] Seifert P *et al* 2021 A high-Tc van der Waals superconductor based photodetector with ultra-high responsivity and nanosecond relaxation time *2D Mater.* **8** 035053
[27] Cao Y *et al* 2015 Quality heterostructures from two-dimensional crystals unstable in air by their assembly in inert atmosphere *Nano Lett.* **15** 4914–21
[28] Ward B, Notte J A and Economou N 2006 Helium ion microscope: a new tool for nanoscale microscopy and metrology *J. Vac. Sci. Technol.* B **24** 2871–4
[29] Cybart S A, Cho E Y, Wong T J, Wehlin B H, Ma M K, Huynh C and Dynes R C 2015 Nano Josephson superconducting tunnel junctions in $YBa_2Cu_3O_{7-\delta}$ directly patterned with a focused helium ion beam *Nat. Nanotech.* **10** 598–602
[30] Müller B, Karrer M, Limberger F, Becker M, Schröppel B, Burkhardt C J, Kleiner R, Goldobin E and Koelle D 2019 Josephson junctions and SQUIDs created by focused helium ion beam irradiation of $YBa_2Cu_3O_7$ *Phys. Rev. Appl.* **11** 044082
[31] Cho E Y, Ma M K, Huynh C, Pratt K, Paulson D N, Glyantsev V N, Dynes R C and Cybart S A 2015 $YBa_2Cu_3O_{7-\delta}$ superconducting quantum interference devices with metallic to insulating barriers written with a focused helium ion beam *Appl. Phys. Lett.* **106** 252601
[32] Chen X K, Zeng Y J and Chen K Q 2020 Thermal transport in two-dimensional heterostructures *Front. Mater.* **7** 578791
[33] Engel A, Renema J J, Il'in K and Semenov A 2015 Detection mechanism of superconducting nanowire single-photon detectors *Supercond. Sci. Technol.* **28** 114003
[34] Jukna A and Sobolewski R 2003 Time-resolved photoresponse in the resistive flux-flow state in Y-Ba-Cu-O superconducting microbridges *Supercond. Sci. Technol.* **16** 911–5
[35] Zhang L *et al* 2014 Characterization of superconducting nanowire single-photon detector with artificial constrictions *AIP Adv.* **4** 067114
[36] Bitauld D, Marsili F, Gaggero A, Mattioli F, Leoni R, Nejad S J, Lévy F and Fiore A 2010 Nanoscale optical detector with single-photon and multiphoton sensitivity *Nano Lett.* **10** 2977–81
[37] Sobolewski R, Verevkin A, Gol'tsman G N, Lipatov A and Wilsher K 2003 Ultrafast superconducting single-photon optical detectors and their applications *IEEE Trans. Appl. Supercond.* **13** 1151–7
[38] Zhao Y G *et al* 2001 Optical Cooper pair breaking spectroscopy of cuprate superconductors *Phys. Rev.* B **63** 132507
[39] Sandilands L J, Reijnders A A, Su A H, Baydina V, Xu Z, Yang A, Gu G, Pedersen T, Borondics F and Burch K S 2014 Origin of the insulating state in exfoliated high-T_C two-dimensional atomic crystals *Phys. Rev.* B **90** 081402
[40] Niratisairak S, Johansen T H, Katouda S and Ishibashi T 2011 Evolution of a hotspot in a thin BSCCO structured film *Physica* C **471** 222–5
[41] Xiao Z L, Andrei E Y and Ziemann P 1998 Coexistence of the hot-spot effect and flux-flow instability in high-T_C superconducting films *Phys. Rev.* B **58** 11185
[42] Lyatti M, Wolff M A, Savenko A, Kruth M, Ferrari S, Poppe U, Pernice W, Dunin-Borkowski R E and Schuck C 2018 Experimental evidence for hotspot and phase-slip mechanisms of voltage switching in ultra-thin $YBa_2Cu_3O_{7-\delta}$ nanowires *Phys. Rev.* B **98** 054505
[43] Polakovic T, Armstrong W, Karapetrov G, Meziani Z E and Novosad V 2020 Unconventional applications of superconducting nanowire single photon detectors *Nanomaterials* **10** 1198